catalysts

MDPI

Article

Mechanochemically Synthesized Supported Magnetic Fe-Nanoparticles as Catalysts for Efficient Vanillin Production

María Dolores Márquez-Medina [1], Daily Rodríguez-Padrón [1], Alina M. Balu [1], Antonio A. Romero [1], Mario J. Muñoz-Batista [1,*] and Rafael Luque [1,2,*]

[1] Departamento de Química Orgánica, Universidad de Córdoba, Campus de Rabanales, Edificio Marie Curie (C-3), Ctra Nnal IV-A, Km 396, E14014, Cordoba, Spain; q92mamem@uco.es (M.D.M.-M.); dailydggs@gmail.com (D.R.-P.) qo2balua@uco.es (A.M.B.); qo1rorea@uco.es (A.A.R.)

[2] Scientific Center for Molecular Design and Synthesis of Innovative Compounds for the Medical Industry, People´s Friendship University of Russia (RUDN University), 6 Miklukho-Maklaya str., 117198 Moscow, Russia

* Correspondence: rafael.luque@uco.es (R.L.), qo2mubam@uco.es (M.J.M.-B.)

Received: 15 February 2019; Accepted: 18 March 2019; Published: 21 March 2019

Abstract: Magnetically separable nanocatalysts were synthesized by incorporating iron nanoparticles on a mesoporous aluminosilicate (Al-SBA-15) through a mechanochemical grinding pathway in a single step. Noticeably, magnetic features were achieved by employing biomass waste as a carbon source, which additionally may confer high oxygen functionalities to the resulting material. The resulting catalysts were characterized using X-ray diffraction, X-ray photoelectron spectroscopy, transmission electron microscopy, scanning electron microscopy, porosimetry, and magnetic susceptibility. The magnetic nanocatalysts were tested in the selective oxidative cleavage reaction of isoeugenol and vanillyl alcohol to vanillin. As a result, the magnetic nanocatalysts demonstrated high catalytic activity, chemical stability, and enormous separation/reusability qualities. The origin of catalytic properties and its relationship with the iron oxide precursor were analyzed in terms of the chemical, morphological, and structural properties of the samples. Such analysis allows, thus, to highlight the superficial concentration of the iron entities and the interaction with Al as key factors to obtain a good catalytic response.

Keywords: magnetic nanoparticles; mechanochemistry; iron oxides; Al-SBA-15; vanillin

1. Introduction

Currently, environmental issues related to global warming [1], which can have a negative impact on human safety, together with the limited reserves of crude oil, motivated the scientific community in the design of sustainable alternatives for materials, chemicals, energy, and fuel production [2,3]. A change is required from the traditional concept of process efficiency focused on chemical performance, considering the premises of sustainable development for the replacement of fossil resources by renewable raw materials. In this regard, biomass valorization represents an attractive option to supply the chemical demand by using an abundant and renewable source [4,5]. Lignocellulosic biomass, mainly composed of lignin, cellulose, and hemicellulose, can lead to terpenes, carbohydrates, fatty esters, and aromatics. In this sense, biomass was recently subject of numerous studies, attracting great interest as the most abundant renewable raw material of organic carbon available on the planet and as a perfect substitute for oil in the production of fuels and chemical products [6–8]. These facts represent at the same time an interesting and challenging topic

for the chemical industry [9]. Therefore, the use of catalytic systems can pave the way for an optimum biomass valorization [10,11].

In particular, the catalytic valorization of biomass-derived compounds such as eugenol, isoeugenol, and ferulic acid was broadly studied through the past few years [12–15]. The molecules may replace petrol-based intermediates, such as guaiacol and glyoxylic acid, for the synthesis of vanillin [16]. The latter compound is a well-known flavoring agent, popular in the food, cosmetic, and pharmaceutical industries. Several catalytic strategies, employing different transition metal oxides, were explored for the conversion of isoeugenol and vanillyl alcohol to vanillin [17,18]. In particular, supported and non-supported iron oxides were extensively applied to isoeugenol valorization [19–21]. However, much more effort should be devoted in order to optimize the catalytic systems and, in turn, to enhance the catalytic performance in terms of conversion, selectivity, and stability.

Nanostructured heterogeneous catalysts possess advantages related to their recovery and reuse, thus contributing to increasing the sustainable credentials of chemical processes [22,23]. In this regard, the use of stable, active, and recyclable materials proved to be very useful for a wide range of chemical processes [24–26]. The deposition of highly active nanoparticles on various organic or inorganic supports is probably the most effective strategy for the reuse of nanocatalysts [27]. The design of magnetic nanocatalyts facilitates a more efficient separation by using a magnetic field, compared to conventional decanting and filtration techniques [28–34].

Iron oxide-based nanomaterials may possess different magnetic features depending on their crystalline phase (e.g., hematite, maghemite, and magnetite) [35]. Magnetic iron oxides are generally obtained by liquid-phase methods, which involve additional solvents and reagents [36]. A novel technique for the synthesis of magnetic nanocatalysts is mechanical grinding (mechanochemistry). In general, this method can avoid the use of toxic organic solvents that could be released to the environment and increase the effectiveness and reproducibility in the synthesis of the materials. Mechanochemistry is a promising alternative for the synthesis of heterogeneous catalysts [37]. Regarding the synthesis of magnetic iron oxide, mechanochemical methods require the use of propionic acid, as previously described by our research group [38,39]. Propionic acid, together with the iron precursor, gives rise to an iron carboxylate compound, which can be further converted via calcination into crystalline magnetic iron-oxide phases. Replacement of such a reagent by a lignocellulosic residue not only results in the desired iron oxide phase, but could also represent a sustainable alternative for these type of materials. Also, textural properties constitute a key factor for a good catalytic performance, such as porosity. Therefore, employing silica mesoporous supports including MCM-41 (Hexagonal), MCM-48 (Cubic pore morphology), SBA-15 (Hexagonal pore morphology), and Al-SBA-15 (Hexagonal pore morphology) for transition-metal oxides can provide access to advanced systems with optimum porosity for catalytic applications [40-42]. Through this work, two strategies are explored for biomass valorization, namely chemical and materials, revealing the underexploited potential of such types of residues to ameliorate the environmental impact of chemical processes.

2. Results and Discussion

The proposed methodology resulted to be effective for the preparation of such catalytic systems, pointing out that mechanochemical protocols represent a green and remarkable pathway to synthesize advanced nanomaterials. Table S1 (Supplementary Materials) summarizes the materials synthesized. In particular, the employment of biomass residue as a carbon source presents outstanding advantages, since it allows the formation of a magnetic phase without employing other chemicals, such as propionic acid, commonly used for the synthesis of magnetic iron oxide [17]. Nanomaterials synthesized employing iron perchlorate and iron chloride did not show magnetic susceptibility. On the other hand, concentrations higher than 40% for iron citrate and higher than 30% for iron nitrate showed remarkable magnetic features. Magnetic susceptibility values were found in the range of 70–210 × 10^{-6} $m^3 \cdot kg^{-1}$ (Table S1, Supplementary Materials). These values are consistent with the content of maghemite in the support since the pure maghemite nanoparticles generally show

magnetic susceptibilities of approximately 500 × 10^{-6} $m^3 \cdot kg^{-1}$ [43]. These susceptibility values allow the magnetic separation from the reaction mixture.

After functionalization with iron oxide, X-ray diffraction (XRD) analysis of the samples prepared with iron citrate (FeMagC) showed a typical diffraction pattern that could be correlated with a mixture of hematite (as the major component) and maghemite phases (Figure 1). The diffraction peaks at 2θ = 30.2°, 33.2°, 35.7°, 40.9°, 49.5°, 54.1°, 57.3°, 62.4°, and 64.1° correspond to (200), (104), (110), (113), (024), (116), (112), (214), and (300) crystallographic planes of hematite phase, respectively [41]. In addition, maghemite-related peaks were observed at 2θ = 24.2° and 43.3°, suggesting the presence of both crystalline phases with a marked hematite prominence. Remarkably, the employment of iron nitrate (FeMagN) resulted in (a) formation of pure maghemite (2θ = 30.2°, 35.5°, 43.5°, 57.5°, and 63.0° associated with (200), (311), (400), (511) and (440)), and (b) loss of crystallinity [44,45]. The presence of the maghemite phase in the samples facilitates further recovery and reuse of the synthesized catalytic systems.

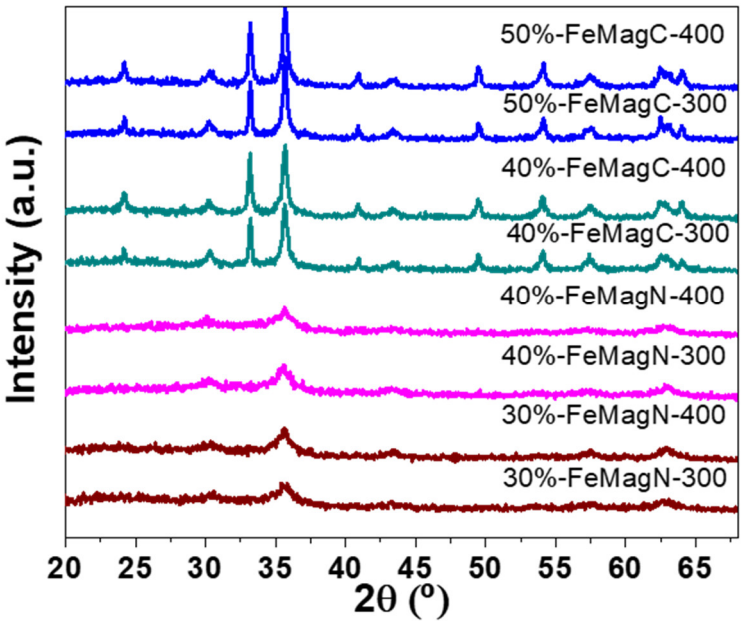

Figure 1. X-ray diffraction (XRD) patterns of selected samples.

Nitrogen adsorption–desorption analysis of selected materials displayed a mesoporous structure in all cases, as can be observed in Figure 2A and B, corresponding to type IV isotherms, according to the International Union of Pure and Applied Chemistry (IUPAC) classification, showing an acute inflection in the P/P_0 range of 0.5–0.8 [46]. A decrease of surface area was observed after incorporation of iron oxide nanoparticles. Brunauer–Emmett–Teller (BET) surface areas around 240–340 $m^2 \cdot g^{-1}$ were obtained (Table 1). Such values are in good agreement with those previously reported for functionalized Al-SBA-15 samples.[47]. In addition, pore diameters and pore volume also showed a decrease of around 50% after functionalization (Table 1). These results can be understood from a partial occlusion of Al-SBA-15 pores in presence of the Fe-oxide co-catalyst. Elemental information about the components of samples was obtained with the help of SEM and energy-dispersive X-ray spectroscopy (EDX). EDX analysis (Table 1) corroborated the presence of the expected elements Al, Si, and Fe, and no significant differences were observed among the studied samples, as may be envisaged by their similar chemical composition (for same iron salt concentration) when different precursors were used. EDX analysis also allowed the identification of bulk N concentration in the samples; however, very low concentrations (in comparison to superficial concentration obtained by X-ray photoelectron spectroscopy (XPS)) and, consequently, high standard errors prevented the analysis of this data. This is an expected result considering that a sacrificial template

mechanochemical-based method was used, in which the waste feedstock is almost completely removed during the calcination process.

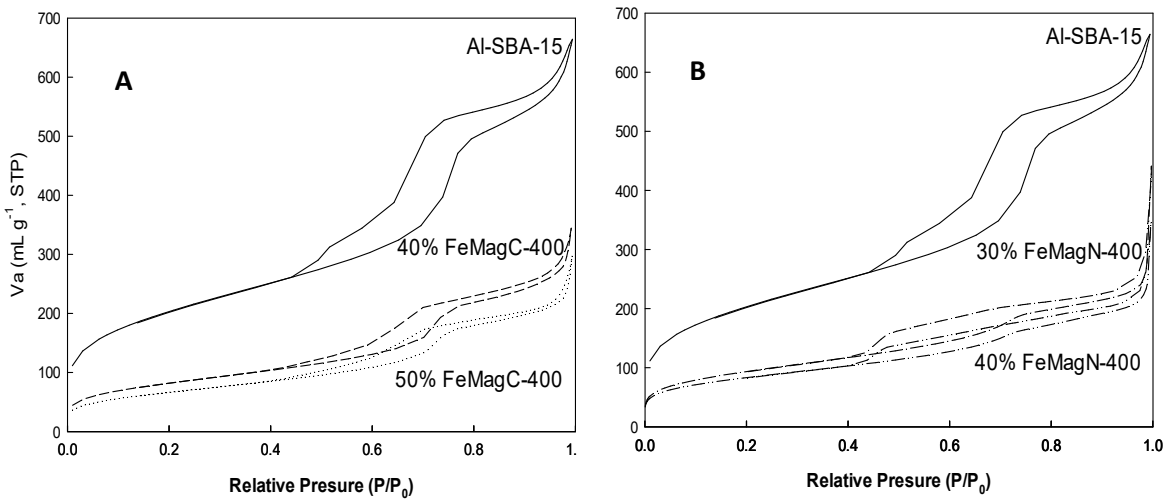

Figure 2. N_2 adsorption–desorption isotherms of **(A)** FeMagC at 400 °C, and **(B)** FeMagN at 400 °C.

Table 1. Textural properties of the obtained materials. BET—Brunauer–Emmett–Teller; EDX—energy-dispersive X-ray spectroscopy.

Catalyst	S_{BET} ($m^2 \cdot g^{-1}$)	Average Pore diameter (nm)*	Average pore volume ($mL \cdot g^{-1}$)	SEM–EDX		
				%Al	%Si	%Fe
Al-SBA-15	736	8.5	0.8	-	-	-
40% FeMagC-400	297	7.5	0.4	3.0	76.1	20.9
50% FeMagC-400	242	7.6	0.3	2.5	70.7	26.8
30% FeMagN-400	339	6.3	0.2	2.6	72.3	25.1
40% FeMagN-400	300	6.4	0.2	2.3	70.6	27.1

Morphological differences between the samples obtained using iron citrate and iron nitrate were further investigated through a TEM study, using 40% FeMagC at 400 °C and 30% FeMagN at 400 °C as representative samples. TEM images of 40% FeMagC at 400 °C and 30% FeMagN at 400 °C (Figures 3A,B) depicted that iron-oxide nanoparticles were successfully incorporated on the Al-SBA-15 surface. In both cases, the Al-SBA-15 support displays its characteristic well-crystallized and porous structure [48]. Also, in both examples, several darker areas, which can be clearly associated with the iron-oxide counterpart, were observed. EDX and TEM analyses support the idea that very close contact between the Al-SBA-15 support and iron-oxide component both at the surface and trapped in the porous structure was generated; however, a heterogeneous distribution of iron-oxide agglomerates also seemed to be present.

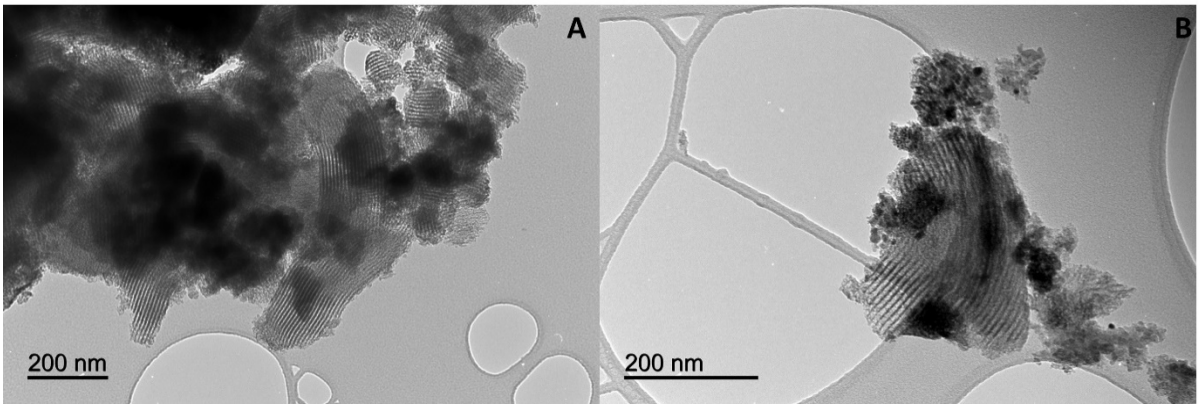

Figure 3. TEM images of (**A**) 40% FeMagC at 400 °C, and (**B**) 40% FeMagN at 400 °C.

In order to provide insight into species at the surface of the material and elucidate their relationship with the precursor used, as well as their influence on the reactions, XPS analysis of the same representative samples (40% FeMagC at 400 °C and 40% FeMagN at 400 °C) was performed. Curve fitting was carried out using the carbon C 1*s* peak (284.6 eV) as a reference for binding energy calibration. The deconvoluted C 1*s* XPS spectra of the obtained materials exhibited three different contributions associated to the presence of C–C/C=C, C–N, and C–O bonds. In particular, the C–N signal detected can be understood most likely due to the presence of nitrogen-containing compounds in the utilized biomass source. In both samples, the presence of Fe^{3+} species could be also inferred from the Fe $2p_{3/2}$ and Fe $2p_{1/2}$ peaks around 710 eV and 725 eV, respectively (Figures 4A,D). XPS spectra did not show the characteristic peaks associated with Fe(II), 709.6 eV or Fe(0), 706.7 eV species [49]. The absence of Fe(II) in the samples, especially, confirmed the formation of maghemite as a magnetic phase instead of magnetite, where both Fe(III) and Fe(II) species are presented [50,51]. Additionally, O 1*s* XPS spectra displayed three different peaks attributed to O–C, O–Fe, and O–Si. In addition, the typical signals of Si 2*p* in SiO_2 were observed at 103.0 eV for both materials. Calculation of Fe/Si ratio was carried out using XPS (Table 2). Interestingly, a comparison with the Fe/Si ratio obtained by EDX (bulk) provides evidence that remarkable superficial differences were obtained using nitrate and citrate precursors. While Fe/Si ratios of the bulk obtained by EDX were essentially unchanged (enhancement factor of 1.4: $(Fe/Si)_{EDX}$ 40% FeMagN at 400 °C/$(Fe/Si)_{EDX}$ 40% FeMagC at 400 °C), the superficial ratio calculated by XPS shows an enhancement factor of 6.2 $(Fe/Si)_{XPS}$ 40% FeMagN at 400 °C/$(Fe/Si)_{XPS}$ 40% FeMagC at 400 °C).

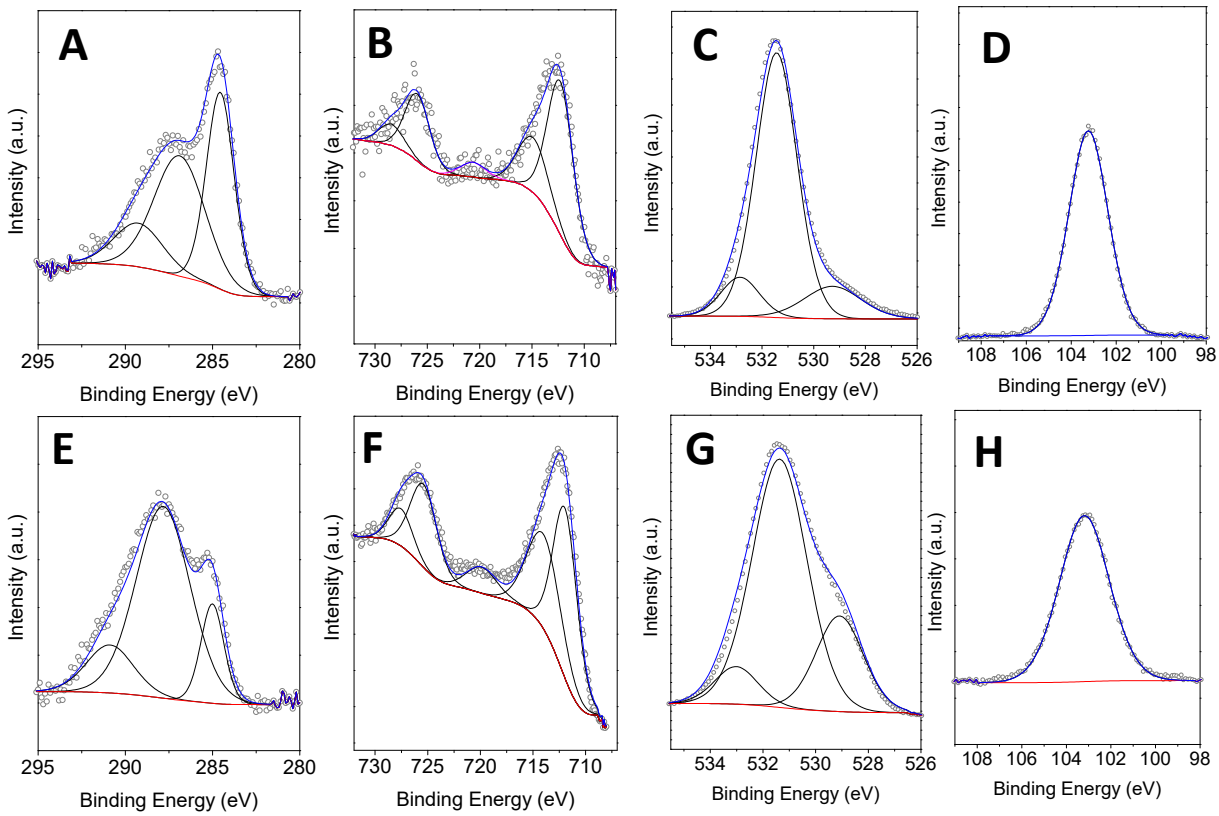

Figure 4. Deconvoluted X-ray photoelectron spectroscopy (XPS) spectra of 40% FeMagC at 400 °C and 40% FeMagN at 400 °C for (**A**,**E**) C 1*s*, (**B**,**F**) Fe 2*p*, (**C**,**G**) O 1*s*, and (**D**,**H**) Si 2*p*.

Table 2. Fe/Si atomic ratio obtained by chemical analysis and X-ray photoelectron spectroscopy (XPS).

Sample	$(Fe/Si)_{XPS}$	$(Fe/Si)_{EDX}$	$(Fe/Si)_{XPS}/(Fe/Si)_{EDX}$
40% FeMagC at 400 °C	0.03	0.3	0.1
40% FeMagN at 400 °C	0.19	0.4	0.5

The catalytic properties of the samples were investigated during the oxidation of isoeugenol and vanillyl alcohol toward the selective production of vanillin (Scheme 1).

Scheme 1. Reaction scheme. (**A**) Oxidation of isoeugenol; (**B**) oxidation of vanillyl alcohol.

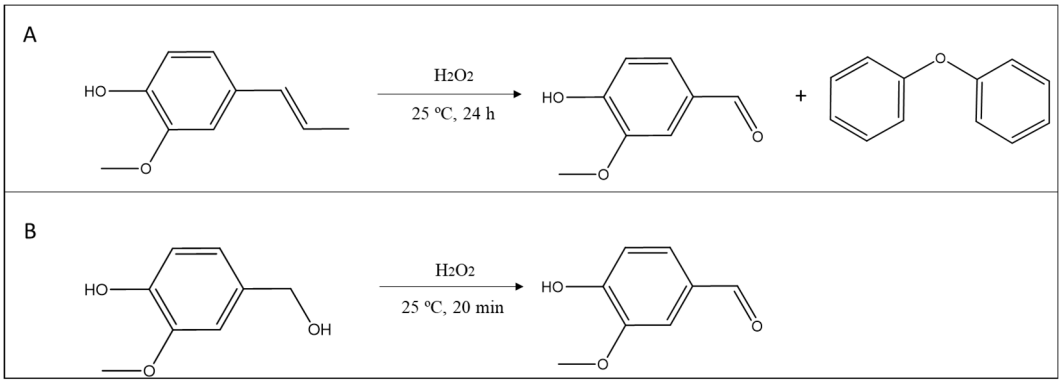

Firstly, control experiments were performed in the absence of the catalysts (blank) and employing Al-SBA-15 as a reference. These control reactions showed negligible activity in the absence of an effective catalytic system (see blank vs. Al-SBA-15 in Figure 5A) for isoeugenol oxidation, obtaining diphenyl structures as the main product. In addition, the vanillyl alcohol oxidation reaction to vanillin showed fair conversions after 2 h of reaction without catalyst and relatively low values when the reference support Al-SBA-15 was used (Figure 5B). The Al-SBA-15 reference is active in the vanillyl alcohol oxidation reaction under used experimental conditions but displays a rather modest activity in comparison with samples containing iron oxide. Under optimized reaction conditions for isoeugenol oxidation [17], prepared nanomaterials showed remarkable differences as a function of the iron precursor. A similar situation was acquired using vanillyl alcohol as a reagent, for which 20 min was settled on as the final reaction time. In both reactions, samples obtained using iron nitrate provided significantly improved conversions in comparison to the series of samples synthesized from iron citrate. In the case of isoeugenol oxidation, the addition of the iron oxide obtained from iron(III) nitrate drove to the highest positive impact in the conversion (more than 80%) regardless of the calcination temperature. As can be seen in Figure 5A, the optimum value of activity was reached using the 40% FeMagN at 400 °C sample. On the other hand, significantly lower conversion values were obtained using ammonium iron(III) citrate as an iron source (~40%). Focusing on selectivity, higher selectivity toward the desired vanillin product was detected for the series FeMagN which confirms the advantages of the use of nitrate instead of the other inorganic salt (Figure 5A). Note that selectivity to vanillin is higher than 70% for the catalyst 30$ MagN at 300 °C and higher than 50% for all samples prepared from nitrate, being higher than previously reported for Fe-containing samples and similar SBA-15-based samples (see Table S2, Supplementary Materials) [19,20]. Diphenylether was the other dominant product of this reaction from which a carbon balance above 95% was obtained for all runs. As presented in Figure 5B, rather similar behavior in terms of activity as a function of the iron precursor was obtained during the vanillyl alcohol oxidation. In this case, full selectivity to vanillin was achieved. Catalysts obtained from nitrate salt showed conversions greater than 99% in the reaction while a worsening of activity was detected using citrate. In addition, calcination temperature modulated the catalytic response of the solid, causing more activity at higher calcination temperature, which does not seem related to the crystallinity of samples (Figure 1). No easy comparison between sample obtained using nitrate or citrate was possible. We, however, previously demonstrated by ^{27}Al NMR that Al-SBA-15 suffers a considerable transformation in contact with Fe_2O_3 entities, which clearly indicates a strong interaction between Fe and Al elements

[52]. In fact, the enhancement of surface acidities presented in Table 3 for Fe-containing samples, measured using pyridine and 2,6-dimethylpyridine, could be associated with Al–Fe interaction. Note that a siliceous sample (Si-SBA-15) did not show measurable acidity properties. Just as important, higher Lewis acidity was obtained when iron nitrate was used as an iron source (while both catalysts synthesized, 40% FeMagN at 400 °C and 40% FeMagN at 400 °C, presented similar Brønsted acid sites), which would favor an enhanced activity.

Table 3. Surface acidity measured at 300 °C as μmol adsorbed of pyridine (PY) or 2,6-dimethylpyridine (DMPY) per gram of sample.

Sample	Surface acidity at 300 °C/μmol·g^{-1}	
	PY (Total acidity)	DMPY (Brønsted acidity)
Si-SBA-15	-	-
Al-SBA-15	82	61
40% FeMagN at 400 °C	290	143
40% FeMagC at 400 °C	155	164

In fact, Al/Fe reduces the binding energy of the Fe–O bond, which, as demonstrated [53], generates more flexible lattice oxygen and reactivity during oxidation reactions [52]. To further analyze the activity of the samples and its relationship with the iron precursor, differences of Fe/Si bulk and superficial ratios can be compared. Data presented in Table 2 clearly describe a correlation in the behavior of the activity (see activity data for 40% FeMagC at 400 °C and 40% FeMagN at 400 °C in Figures 5A,B) and superficial iron entities exposed (measured as Fe/Si ratio obtained by XPS) for the catalytic process using the 40% FeMagC at 400 °C and 40% FeMagN at 400 °C samples. This means that, although the use of nitrate instead of citrate seems to produce slightly better interaction with the porous structure of the Al-SBA-15, these differences cannot be considered significant (see Tables 1 and 2). On the other hand, the Fe/Si ratio obtained by XPS indicates a significant increase of the superficial concentration of iron oxide of the nitrate series in comparison with samples obtained from citrate, which, according to activity data of Figure 4, would define the differences between both groups of catalysts (FeMagN vs. FeMagC).

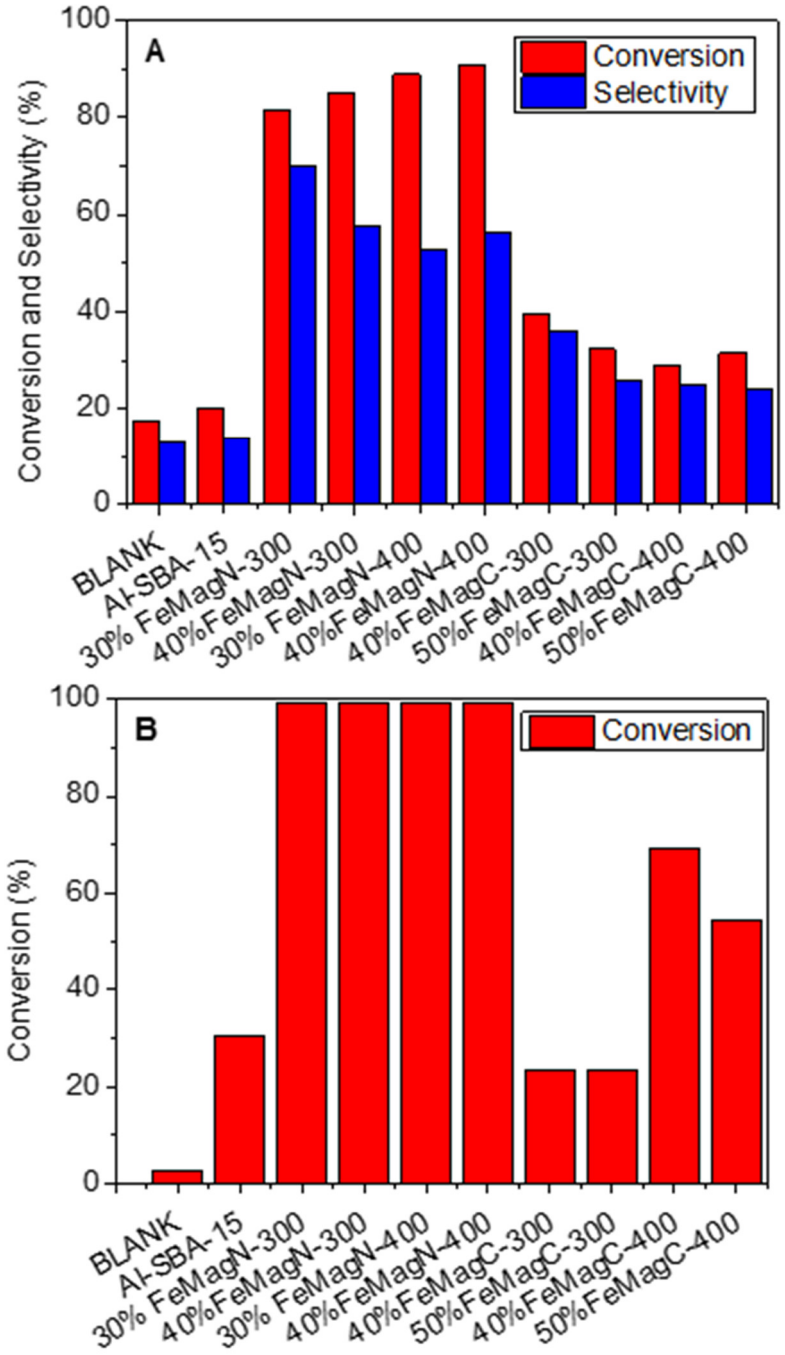

Figure 5. Catalytic conversion and vanillin selectivity (for isoeugenol reaction) for both oxidation reactions at 25 °C, 1 atm. (**A**) Oxidation of isoeugenol at 24 h; (**B**) oxidation of vanillyl alcohol at 20 min. The blank was measured after 2 h of reaction.

A reusability study of representative samples suggested a relatively high stability of the synthesized catalysts obtained by mechanochemistry. These measurements were performed employing one of the most active catalytic systems, namely 30% FeMagN at 400 °C (Figures 6A, B) and cycles of 24 h and 20 min for isoeugenol and vanillyl alcohol, respectively. For the isoeugenol oxidation reaction (Figure 6A), after a decrease of the activity (from 77% to 53% conversion), the catalytic properties remained essentially unchanged. As shown in Figure 6A, after the first cycle (24 h of reaction), approximately 25% conversion was lost. However, a reactivation of the activity can be easily obtained by calcinating the catalyst at 400 °C. A very similar conversion and selectivity, in comparison with the first use of the catalyst, was obtained after the calcination treatment (80% and

60% conversion and selectivity to vanillin, respectively), suggesting that deactivation of the sample was not due to potential iron-oxide leaching, but to the presence of poisoning surface compounds, which is a common phenomenon under batch conditions and long reaction times. Furthermore, much less catalytic deactivation was observed during the oxidation of vanillyl alcohol under the used experimental conditions (Figure 6B, see caption for details), which can also be understood taking into account that significantly shorter reaction times were used. Similarly, a simple calcination post-treatment (400 °C) was demonstrated to be an effective process to reactivate the catalyst (Figure 6B).

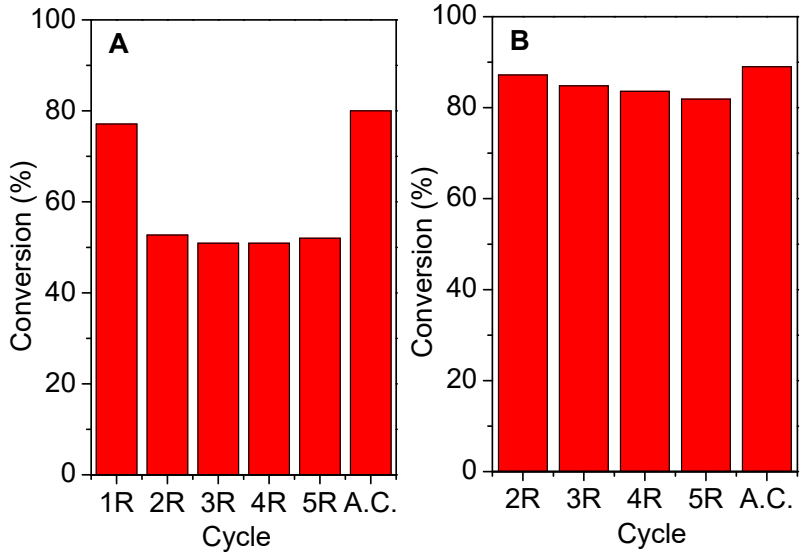

Figure 6. Reuses of the 30% FeMagN at 400 °C for both oxidation reactions at 25 °C, 1 atm. (**A**) Oxidation of isoeugenol; each cycle was 24 h of reaction; (**B**) oxidation of vanillyl alcohol; each cycle was 20 min of reaction. A.C.: reused catalyst after calcination.

3. Materials and Methods

3.1. Synthesis of Al-SBA-15

The preparation of the mesoporous aluminosilicate (Al-SBA-15, molar ratio Si/Al = 20) was carried out according to a procedure reported by Stucky et al. [42]. In particular, Pluronic, P123 triblock copolymer, Sigma-Aldrich, Madrid, Spain (20.6 g) was dissolved in 750 mL of HCl (Panreac, Barcelona, Spain) solution (0.2 M, pH = 1.5), by stirring at 40 °C for 2 h. Tetraethyl orthosilicate (TEOS), Sigma-Aldrich, Madrid, Spain (25 mmol) and aluminum isopropoxide, Sigma-Aldrich, Madrid, Spain (10 mmol) were then added to the mixture and further stirred for 24 h at 40 °C. Subsequently, the solution was transferred to a 100-mL autoclave at 100 °C for 24 h. The obtained material was filtered, dried at 60 °C, and finally calcined at 600 °C for 2 h.

3.2. Synthesis of Catalysts

The synthesis of the nanocatalysts was carried out by means of a mechanochemical milling process using Al-SBA-15 as the support, biomass (a lignocellulosic-derived residue) as the carbon source, and different iron precursors (ammonium iron(III) citrate (Sigma-Aldrich, Madrid, Spain), iron(III) nitrate (Sigma-Aldrich, Madrid, Spain), iron(III) perchlorate hydrate (Panreac, Barcelona, Spain), and iron(III) chloride, (Sigma-Aldrich, Madrid, Spain). For the catalyst preparation, Al-SBA-15 support (2 g) and organic waste (1 g) were introduced into the planetary ball mill jar, where the different iron salts used in percentages by weight of 10, 20, 30, 40, and 50 were introduced. The synthesis mixture was ground for 10 min at 350 rpm using 18 stainless-steel balls of 10 mm × 1 cm. The material obtained after the grinding process was calcined at three different temperatures, namely

300, 400, and 500 °C. The nanomaterials obtained were denoted as X-FeMagY-Z, where X = theoretical content by weight of iron present, Y = iron precursor salt (C = ammonium iron(III) citrate, N = iron(III) nitrate, P = iron(III) perchlorate hydrate, and Cl = iron(III) chloride), and Z = calcination temperature.

3.3. Characterization Techniques

Nanocatalysts were characterized by several techniques, including X-ray diffraction (XRD), X-ray photoelectron spectroscopy (XPS), scanning electron microscopy with energy-dispersive X-ray spectroscopy (SEM-EDX), transmission electron microscopy (TEM), and N_2 physisorption. Additionally, magnetic susceptibility values were additionally determined, in order to confirm the magnetic properties of the prepared materials. X-ray diffraction analysis was carried out on a Bruker D8-Advanced Diffractometer (40 kV, 40 mA) with a Cu X-ray tube (λ = 0.15406) and a goniometer Bragg Bretano θ/θ (Bruker AXS, Karlsruhe, Germany). XRD patterns were acquired in a 10–80° range, at a step size of 0.02° with a counting time per step of 20 s. XPS experiments were carried out in an ultra-high vacuum (UHV) multipurpose surface analysis system Specs™, equipped with the Phoibos 150-MCD energy detector (Berlin, Germany). The sample was previously evacuated overnight under vacuum (<10^{-6} torr). The measurement was accomplished at pressures <10^{-10} mbar, employing a conventional X-ray source (XR-50, Specs (Berlin, Germany), Mg-Kα, hv = 1253.6 eV, 1 eV = 1.603 × 10^{-19} J) in a "stop and go" mode. The XPS CASA program (Casa Software Ltd., Cheshire, UK) was used to obtain the deconvolution of the curves and the element quantification. TEM micrographs were acquired in a FEI Tecnai G2 system, equipped with a charge-coupled device (CCD) camera. Samples were previously suspended in ethanol and subsequently deposited on a copper grid. Element quantification of the catalysts was obtained using a JEOL JSM 7800F (JEOL Ltd., Akishima, Tokyo, Japan) scanning electron microscope equipped with an Inca Energy 250 microanalysis system, Si/Li type window detector (ATW2), detection range from boron to uranium, and resolution of 137 eV to 5.9 keV. The adsorption/desorption isotherms of N_2 were determined in the Micromeritics automatic analyzer ASAP 2000 (Micromeritics Instrument Corp., Norcross, GA, USA). at −196 °C. Samples were previously degassed overnight at 130 °C under vacuum (P < 10^{-2} Pa). The linear determination of the BET equation was carried out to obtain specific surface areas. Magnetic susceptibility of samples was determined by using a MS2 magnetic susceptibiliser, (Bartington Instruments Ltd., Witney, UK), at room temperature using the dual frequency MS2B (Bartington Instruments Ltd., Witney, UK) laboratory sensor (470 and 4700 Hz). Surface acidity of the samples was measured using pyridine (PY) and 2,6-dimethylpyridine (DMPY) as titrant bases, since they are essentially adsorbed on both types of acidic sites, Brønsted and Lewis and Brønsted acid sites, respectively, at 250 °C (50 °C below the calcination temperature during the synthesis of the samples). The pulses were carried out by means of a microinjector, in the catalytic bed, from a cyclohexane solution of the titrant (0.989 M PY and 0.956 M DMPY). The catalyst was standardized at each titration in a dehydrated and deoxygenated nitrogen flow (50 mL·min^{-1}) (99.999% purity) at 250 °C. The catalyst used (~0.03 g) was fixed by means of Pyrex glass wool stoppers, inside a stainless-steel tubular microreactor of 4 mm internal diameter. The injected base was analyzed by gas chromatography with a flame ionization detector (FID), using an analytical column 0.5 m in length, containing 5% by weight of polyphenylether in Chromosorb AW-MCS 80/100 (Supelco Analytical, Bellefonte, PA, USA).

3.4. Catalytic Activity

The production of vanillin was carried out by conventional heating using isoeugenol and vanillyl alcohol as reagents. The selective oxidative cleavage of isoeugenol to vanillin was carried out using a multiple parallel reaction system (Carrusel Reaction Station™, Radleys Discovery Technologies Ltd., Saffron Walden, United Kingdom) at 25 °C, employing isoeugenol (0.8 g, 5 mmol), 33% hydrogen peroxide (1.2 mL, 11.7 mmol) as an oxidant agent, acetonitrile as a solvent (8 mL, 153 mmol), and 10 mol.% catalyst. In addition, oxidation of vanillyl alcohol to vanillin was carried out, using vanillyl alcohol (0.8 g, 5 mmol), hydrogen peroxide, 30 wt.% in water (1.2 mL, 11.7 mmol), acetonitrile (8 mL, 153 mmol), and 10 mol.% catalyst.

The progress of the reaction was evaluated by gas chromatography (GC) employing an Agilent Technologies 7890 A GC System (Madrid, Spain) equipped with a Petrocol™ DH column (100m×0.25mm×0.50 μm) and a flame ionization detector (FID).

4. Conclusions

A simple and reproducible process for the synthesis of iron nanoparticles deposited on Al-SBA-15 using biomass waste was developed. The nanomaterials possess suitable structural and textural properties for their subsequent use as catalysts, as well as magnetic properties that allow easy separation from the reaction media. The catalytic performance of such noncatalytic systems shows promising results for the selective production of vanillin toward isoeugenol and vanillyl alcohol oxidation at room temperature in conventional liquid phase. Conversions in the range of 80% to 90% molar, with selectivities ≥50% molar were achieved. Results suggested that the Al–Fe interaction and the subsequent enhancement of Lewis acid sites, as well as more iron-oxide species superficially available for the oxidation process, are the most important factors to obtain high activity and vanillin selectivity using the nitrate salt.

Acknowledgments: The authors gratefully acknowledge support from MINECO under project CTQ2016-78289-P, co-financed with FEDER funds. Mario J. Munoz-Batista gratefully acknowledges MINECO for a JdC contract (Ref. FJCI-2016-29014). This publication was prepared with support from RUDN University Program 5-100.

Funding: This research was funded by MINECO, CTQ2016-78289-P, FJCI-2016-29014 and RUDN University Program 5-100.

Conflicts of Interest: The authors declare no conflict of interest.

References

1. Sang, W.; Bai, F. Vascular diversity patterns of forest ecosystem before and after a 43-year interval under changing climate conditions in the Changbaishan Nature Reserve, northeastern China. In *Forest Ecology*; Springer: Berlin, Germany, 2008; Volume 201, pp. 115–130.
2. Clark, J.H.; Luque, R.; Matharu, A.S. Green chemistry, biofuels, and biorefinery. *Annu. Rev. Chem. Biomol. Eng.* **2012**, *3*, 183–207.
3. Liao, S.; Wang, F.; Wu, T.; Pan, W. Crude oil price decision under considering emergency and release of strategic petroleum reserves. *Energy* **2016**, *102*, 436–443.
4. Tuck, C.O.; Pérez, E.; Horváth, I.T.; Sheldon, R.A.; Poliakoff, M. Valorization of biomass: Deriving more value from waste. *Science* **2012**, *337*, 695–699.
5. Ragauskas, A.J.; Beckham, G.T.; Biddy, M.J.; Chandra, R.; Chen, F.; Davis, M.F.; Davison, B.H.; Dixon, R.A.; Gilna, P.; Keller, M. Lignin valorization: Improving lignin processing in the biorefinery. *Science* **2014**, *344*, 1246843.
6. Corma, A.; Iborra, S.; Velty, A. Chemical routes for the transformation of biomass into chemicals. *Chem. Rev.* **2007**, *107*, 2411–2502.
7. Ragauskas, A.J.; Williams, C.K.; Davison, B.H.; Britovsek, G.; Cairney, J.; Eckert, C.A.; Frederick, W.J.; Hallett, J.P.; Leak, D.J.; Liotta, C.L. The path forward for biofuels and biomaterials. *Science* **2006**, *311*, 484–489.
8. Stöcker, M. Biofuels and biomass to liquid fuels in the biorefinery: Catalytic conversion of lignocellulosic biomass using porous materials. *Angew. Chem. Int. Ed.* **2008**, *47*, 9200–9211.
9. Filiciotto, L.; Luque, R. Biomass Promises: A Bumpy Road to a Renewable Economy. *Curr. Green Chem.* **2018**, *5*, 47–59.
10. Rodríguez-Padrón, D.; Puente-Santiago, A.R.; Balu, A.M.; Muñoz-Batista, M.J.; Luque, R. Environmental Catalysis: Present and Future. *ChemCatChem* **2018**, *11*, 18–38.
11. Polshettiwar, V.; Varma, R.S. Green chemistry by nano-catalysis. *Green Chem.* **2010**, *12*, 743–754.
12. Franco, A.; De, S.; Balu, A.M.; Romero, A.A.; Luque, R. Selective oxidation of isoeugenol to vanillin over mechanochemically synthesized aluminosilicate supported transition metal catalysts. *ChemistrySelect* **2017**, *2*, 9546–9551.
13. Filiciotto, L.; Balu, A.M.; Romero, A.A.; Rodríguez-Castellón, E.; van der Waal, J.C.; Luque, R. Benign by design preparation of humin-based iron oxide catalytic nanocomposites. *Green Chem.* **2017**, *19*, 4423–4434.

14. Chen, C.L.; Chang, H.M.; Kirk, T.K. Aromatic acids produced during degradation of lignin in spruce wood by Phanerochaete chrysosporium. *Holzforsch. Int. J. Biol. Chem. Phys. Technol. Wood* **1982**, *36*, 3–9.
15. Gallage, N.J.; Møller, B.L. Vanillin–bioconversion and bioengineering of the most popular plant flavor and its de novo biosynthesis in the vanilla orchid. *Mol. Plant* **2015**, *8*, 40–57.
16. Lampman, G.M.; Sharpe, S.D. A phase transfer catalyzed permanganate oxidation: Preparation of vanillin from isoeugenol acetate. *J. Chem. Educ.* **1983**, *60*, 503.
17. Márquez-Medina, M.D.; Prinsen, P.; Li, H.; Shih, K.; Romero, A.A.; Luque, R. Continuous-Flow Synthesis of Supported Magnetic Iron Oxide Nanoparticles for Efficient Isoeugenol Conversion into Vanillin. *ChemSusChem* **2018**, *11*, 389–396.
18. Geng, L.; Zheng, B.; Wang, X.; Zhang, W.; Wu, S.; Jia, M.; Yan, W.; Liu, G. Fe_3O_4 nanoparticles anchored on carbon serve the dual role of catalyst and magnetically recoverable entity in the aerobic oxidation of alcohols. *ChemCatChem* **2016**, *8*, 805–811.
19. Saberi, F.; Rodríguez-Padrón, D.; Doustkhah, E.; Ostovar, S.; Franco, A.; Shaterian, H.R.; Luque, R. Mechanochemically modified aluminosilicates for efficient oxidation of vanillyl alcohol. *Catal. Commun.* **2019**, *118*, 65–69.
20. Saberi, F.; Rodriguez-Padrón, D.; Garcia, A.; Shaterian, H.R.; Luque, R. Unprecedented Proline-Based Heterogeneous Organocatalyst for Selective Production of Vanillin. *Catalysts* **2018**, *8*, 167.
21. Fache, M.; Boutevin, B.; Caillol, S. Vanillin production from lignin and its use as a renewable chemical. *ACS Sustain. Chem. Eng.* **2015**, *4*, 35–46.
22. Zhang, K.; Hong, K.; Suh, J.M.; Lee, T.H.; Kwon, O.; Shokouhimehr, M.; Jang, H.W. Facile synthesis of monodispersed Pd nanocatalysts decorated on graphene oxide for reduction of nitroaromatics in aqueous solution. *Res. Chem. Intermed.* **2019**, *45*, 599–611.
23. Zhang, K.; Suh, J.M.; Choi, J.W.; Jang, H.W.; Shokouhimehr, M.; Varma, R.S. Recent Advances in the Nanocatalyst-Assisted NaBH4 Reduction of Nitroaromatics in Water. *ACS Omega* **2019**, *4*, 483–495.
24. Lu, F.; Ruiz, J.; Astruc, D. Palladium-dodecanethiolate nanoparticles as stable and recyclable catalysts for the Suzuki-Miyaura reaction of aryl halides under ambient conditions. *Tetrahedron Lett.* **2004**, *45*, 9443–9445.
25. Astruc, D. *Transition-Metal Nanoparticles in Catalysis: From Historical Background to the State of the Art*; Wiley-VCH Verlag Gmbh & Co.: Weinheim, Germany, 2008, Volume 1, pp. 1–48.
26. Shokouhimehr, M.; Shin, K.-Y.; Lee, J.S.; Hackett, M.J.; Jun, S.W.; Oh, M.H.; Jang, J.; Hyeon, T. Magnetically recyclable core–shell nanocatalysts for efficient heterogeneous oxidation of alcohols. *J. Mater. Chem. A* **2014**, *2*, 7593–7599.
27. Alamgholiloo, H.; Zhang, S.; Ahadi, A.; Rostamnia, S.; Banaei, R.; Li, Z.; Liu, X.; Shokouhimehr, M. Synthesis of bimetallic 4-PySI-Pd@ Cu (BDC) via open metal site Cu-MOF: Effect of metal and support of Pd@ Cu-MOFs in H2 generation from formic acid. *Mol. Catal.* **2019**, *467*, 30–37.
28. Iranmanesh, M.; Hulliger, J. Magnetic separation: Its application in mining, waste purification, medicine, biochemistry and chemistry. *Chem. Soc. Rev.* **2017**, *46*, 5925–5934.
29. Kainz, Q.M.; Reiser, O. Polymer and dendrimer coated magnetic nanoparticles as versatile supports for catalysts, scavengers, and reagents. *Acc. Chem. Res.* **2014**, *47*, 667–677.
30. Shokouhimehr, M. Magnetically separable and sustainable nanostructured catalysts for heterogeneous reduction of nitroaromatics. *Catalysts* **2015**, *5*, 534–560.
31. Choi, K.H.; Shokouhimehr, M.; Sung, Y.E. Heterogeneous Suzuki cross-coupling reaction catalyzed by magnetically recyclable nanocatalyst. *Bull. Korean Chem. Soc.* **2013**, *34*, 1477–1480.
32. Jun, S.W.; Shokouhimehr, M.; Lee, D.J.; Jang, Y.; Park, J.; Hyeon, T. One-pot synthesis of magnetically recyclable mesoporous silica supported acid–base catalysts for tandem reactions. *Chem. Commun.* **2013**, *49*, 7821–7823.
33. Shokouhimehr, M.; Lee, J.E.; Han, S.I.; Hyeon, T. Magnetically recyclable hollow nanocomposite catalysts for heterogeneous reduction of nitroarenes and Suzuki reactions. *Chem. Commun.* **2013**, *49*, 4779–4781.
34. Rafiaei, S.M.; Kim, A.; Shokouhimehr, M. Gadolinium triflate immobilized on magnetic nanocomposites as recyclable Lewis acid catalyst for acetylation of phenols. *Nanosci. Nanotechnol. Lett.* **2014**, *6*, 309–313.
35. Rodríguez-Padrón, D.; Balu, A.M.; Romero, A.A.; Luque, R. New bio-nanocomposites based on iron oxides and polysaccharides applied to oxidation and alkylation reactions. *Beilstein J. Org. Chem.* **2017**, *13*, 1982.
36. Shokouhimehr, M.; Hong, K.; Lee, T.H.; Moon, C.W.; Hong, S.P.; Zhang, K.; Suh, J.M.; Choi, K.S.; Varma, R.S.; Jang, H.W. Magnetically retrievable nanocomposite adorned with Pd nanocatalysts: Efficient reduction of nitroaromatics in aqueous media. *Green Chem.* **2018**, *20*, 3809–3817.

37. Muñoz-Batista, M.J.; Rodríguez-Padrón, D.; Puente-Santiago, A.R.; Luque, R. Mechanochemistry: Toward sustainable design of advanced nanomaterials for electrochemical energy storage and catalytic applications. *ACS Sustain. Chem. Eng.* **2018**, *6*, 9530–9544.
38. Ouyang, W.; Yépez, A.; Romero, A.A.; Luque, R. Towards industrial furfural conversion: Selectivity and stability of palladium and platinum catalysts under continuous flow regime. *Catal. Today* **2018**, *308*, 32–37.
39. Pineda, A.; Balu, A.M.; Campelo, J.M.; Romero, A.A.; Carmona, D.; Balas, F.; Santamaria, J.; Luque, R. A Dry Milling Approach for the Synthesis of Highly Active Nanoparticles Supported on Porous Materials. *ChemSusChem* **2011**, *4*, 1561–1565.
40. Linares, N.; Silvestre-Albero, A.M.; Serrano, E.; Silvestre-Albero, J.; García-Martínez, J. Mesoporous materials for clean energy technologies. *Chem. Soc. Rev.* **2014**, *43*, 7681–7717.
41. Shokouhimehr, M.; Asl, M.S.; Mazinani, B. Modulated large-pore mesoporous silica as an efficient base catalyst for the Henry reaction. *Res. Chem. Intermed.* **2018**, *44*, 1617–1626.
42. Zhao, D.; Feng, J.; Huo, Q.; Melosh, N.; Fredrickson, G.H.; Chmelka, B.F.; Stucky, G.D. Triblock copolymer syntheses of mesoporous silica with periodic 50 to 300 angstrom pores. *Science* **1998**, *279*, 548–552.
43. Peters, C.; Dekkers, M.J. Selected room temperature magnetic parameters as a function of mineralogy, concentration and grain size. *Phys. Chem. Earth Parts A/B/C* **2003**, *28*, 659–667.
44. Jia, C.; Sun, L.; Yan, Z.; You, L.; Luo, F.; Han, X.; Pang, Y.; Zhang, Z.; Yan, C. Single-crystalline iron oxide nanotubes. *Angew. Chem.* **2005**, *117*, 4402–4407.
45. Park, J.; Lee, E.; Hwang, N.; Kang, M.; Kim, S.C.; Hwang, Y.; Park, J.; Noh, H.; Kim, J.; Park, J. One nanometer scale size controlled synthesis of monodisperse magnetic Iron oxide nanoparticles. *Angew. Chem.* **2005**, *117*, 2932–2937.
46. Gregg, S.J.; Sing, K.S.W. *A Surface Area and Porosity*; Academic Press: Cambridge, MA, USA, 1982.
47. Rajabi, F.; Fayyaz, F.; Luque, R. Cytosine-functionalized SBA-15 mesoporous nanomaterials: Synthesis, characterization and catalytic applications. *Microporous Mesoporous Mater.* **2017**, *253*, 64–70.
48. Yépez, A.; De, S.; Climent, M.S.; Romero, A.A.; Luque, R. Microwave-assisted conversion of levulinic acid to γ-valerolactone using low-loaded supported iron oxide nanoparticles on porous silicates. *Appl. Sci.* **2015**, *5*, 532–543.
49. Wagner, C.D.; Riggs, W.M.; Davis, L.E.; Moulder, J.F. *Handbook of X-ray Photoemission Spectra*; Perkin-Elmer: Waltham, MA, USA, 1976.
50. Rodríguez-Padrón, D.; Puente-Santiago, A.R.; Caballero, A.; Balu, A.M.; Romero, A.A.; Luque, R. Highly efficient direct oxygen electro-reduction by partially unfolded laccases immobilized on waste-derived magnetically separable nanoparticles. *Nanoscale* **2018**, *10*, 3961–3968.
51. Rodríguez-Padrón, D.; Puente-Santiago, A.R.; Balu, A.M.; Romero, A.A.; Luque, R. Solventless mechanochemical preparation of novel magnetic bioconjugates. *Chem. Commun.* **2017**, *53*, 7635–7637.
52. Balu, A.M.; Pineda, A.; Yoshida, K.; Campelo, M.; Gai, P.L.; Angel, A. Fe/Al synergy in Fe_2O_3 nanoparticles supported on porous aluminosilicate materials : Excelling activities in oxidation reactions. *Chem. Commun.* **2010**, *46*, 7825–7827.
53. Mounzer, H. Heterogeneous Oxidation of Alcohols. Ph.D. Thesis, University of Birmingham, Birmingham, UK, 2009.